npj | 2D materials and applications

www.nature.com/npj2dmaterials

ARTICLE OPEN

Check for updates

Van der Waals enabled formation and integration of ultrathin high-κ dielectrics on 2D semiconductors

Matej Sebek[1,2,5]✉, Zeng Wang[1,5], Norton Glen West[1,3], Ming Yang[4]✉, Darren Chi Jin Neo[1], Xiaodi Su[1], Shijie Wang[1], Jisheng Pan[1], Nguyen Thi Kim Thanh[2]✉ and Jinghua Teng[1]✉

A thin dielectric layer is an important constituent element in 2D materials-based electronics and photonics. Current methods of using hexagonal boron nitride (hBN) and direct deposition of dielectric layer induce either high leakage current or unintentional doping and defect. Here we report a technique for damaging free integration of dielectric layer to form high-quality van der Waals (vdW) heterostructure. The dielectric layer is grown by atomic layer deposition (ALD) on 2D materials and then deterministically transferred on the target 2D material. The much weaker binding energy between the ALD dielectric and the 2D materials enables the growth and exfoliation of the atomically thin dielectrics, which is confirmed by the X-ray photoelectron spectroscopy analyses and the density function theory calculations. The effectiveness of the technology is proven by the Raman and photoluminescence measurement on WS_2 monolayer protected by the dielectric film through harsh plasma treatment. Furthermore, a 2D materials-based MOSFET is constructed as a demonstration of the viability of the technology for electronic device applications. The method produces flat surfaces and clean interfaces and would greatly benefit electronic and photonic applications as encapsulation or high-κ gate dielectric.

npj 2D Materials and Applications (2024)8:9 ; https://doi.org/10.1038/s41699-024-00443-2

INTRODUCTION

Since the discovery of graphene[1], 2D materials and van der Waals (vdW) heterostructure based devices have attracted tremendous interests[2] for their potentials in integration into Si technology[3], formation of monolithic 3D integrated devices featuring multiple components on a single wafer[4], creation of valleytronics[5], optical tunability[6], or applications in metaoptics[7]. However, one pressing challenge that needs to be addressed is the damage-free integration of high-quality thin layers of dielectric materials[2,4,8].

Reliable and facile methods for deterministic placement of 2D material flakes and their stacking are essential for 2D materials research and development. Transfer methods using wedging with liquid[9], hot pick-up with polypropylene carbonate and hexagonal boron nitride (hBN)[10], exfoliation on water-soluble sacrificial layer[11], and most notably transfer using polydimethylsiloxane (PDMS)[12] have been commonly used. While exfoliation and transfer are typically used in laboratory practice, successful scale-up by automatized robotic assembly[13] or wafer-sized transfer[14] have been shown. The large-scale exfoliation and assembly of 2D materials into heterostructures have been progressing rapidly with many important works reported. For example, large-scale integration of 2D heterostructures and devices was demonstrated by using the wafer bonding technique[15]. A common problem of bubble generation at the vdW interface during the transfer can be mitigated by conducting the transfer in a vacuum[16]. Very recently methods to exfoliate 2D materials in cm sizes have been developed and reported by various groups[17–19]. Furthermore, deterministic transfer allows transfer of patterns[10,20,21] and even non-destructive contact engineering[22,23]. A growth and exfoliation of layered hexagonal phase metal oxides from metal substrates have been demonstrated recently[24].

So far, hBN is the most commonly used insulating material for vdW devices. It has been widely employed to enhance the mobility of graphene-based devices[11] and to improve photoluminescence (PL) and electronic properties of transition metal dichalcogenides (TMDC) based devices[25,26]. While hBN can be theoretically exfoliated down to a single layer, in practice, precise control of thickness is challenging and requires a tedious process of trial and error since the optical contrast is much weaker than that of TMDCs or graphene[27].

More importantly, as the defects in hBN lead to a high leakage current[28], its usage as a gate dielectric for electronic devices has been limited. Theoretical calculations have shown that even defect-free hBN is unsuitable as a gate dielectric in particular for scaled devices with ultrathin gates[29]. It is necessary to find other materials such as high-κ oxides as a gate dielectric for future 2D-based integrated circuit fabrication. These materials including Al_2O_3 or HfO_2 are typically grown by ALD, in which the substrate is alternately exposed to pulses of precursors to grow a (sub) monolayer of the material in each cycle[30]. That makes ALD an excellent technique for the deposition of dielectrics with precise control of thickness.

Due to the lack of dangling bonds in 2D materials, ALD using H_2O as an oxygen precursor results in a non-uniform and island-like growth on defects or step edges of 2D materials, which results in leakage current in devices formed[31,32]. This can be overcome by utilizing physisorbed ozone[33] or hydrogen[34] pretreatment to provide additional dangling bonds for uniform and homogeneous growth. However, ozone may either lead to a damage of the 2D

[1]Institute of Materials Research and Engineering, Agency for Science, Technology and Research, Fusionopolis Way 2, Singapore 138634, Singapore. [2]Biophysics Group, Department of Physics & Astronomy, University College London, Gower Street, London WC1E 6BT, UK. [3]Department of Biochemistry and Chemistry, La Trobe Institute for Molecular Science, La Trobe University, Melbourne, Victoria 3086, Australia. [4]Department of Applied Physics, The Hong Kong Polytechnic University, Hung Hom, Hong Kong SAR, China. [5]These authors contributed equally: Matej Sebek, Zeng Wang. ✉email: matej.sebek.17@ucl.ac.uk; kevin.m.yang@polyu.edu.hk; ntk.thanh@ucl.ac.uk; jh-teng@imre.a-star.edu.sg

material[35] or to unintentional doping[36]. Even though ALD is typically more gentle than other alternative dielectric deposition techniques, such as sputtering or e-beam evaporation, the doping leads to PL quenching and alteration of the material's electronic properties[37,38]. Another option is to deposit a thin metal seed layer, which oxidizes and allows ALD deposition of the dielectric[39,40]. However, this is known to decrease the mobility of the devices and may damage atomically thin 2D semiconductors[41]. Furthermore, the conformal deposition nature of ALD makes lift-off challenging for nano-device fabrication[42]. Recently, two studies have shown an integration of high-κ perovskite into van der Waals devices[43,44]. However, they utilize a sacrificial $Sr_3Al_2O_6$ layer between two $SrTiO_3$ films and are thus limited by the roughness of the template $SrTiO_3$. Furthermore, the method requires solvent processing limiting the cleanliness of the interface, which is another critical challenge[45].

Here we report damage-free incorporation of 2D dielectric layers into vdW heterostructures and devices. The dielectric thin film is grown on a 2D film using the ALD growth recipe we developed and then transferred to the targeted vdW structures, by utilizing the weaker bonding energy between 2D material and the ALD dielectrics. Our method utilizing exfoliation and deterministic transfer circumvents the commonly faced problems of unintentional doping and damaging of the underlying materials by depositing dielectric directly on the targeted vdW structures. It is a clean and all-dry process that does not require any solvents. Moreover, our method can extend to the deterministic transfer of a range of materials with different dielectric functions, which would benefit the fast-developing 2D vdW heterostructure research and device application in electronics and photonics.

RESULTS

Description of the method

The detailed process of the ultrathin dielectric integration into vdW heterostructure is illustrated in Fig. 1. The layered material is exfoliated on PDMS (Fig. 1a). We demonstrate the applicability of the method with two different layered materials - graphite and WSe_2, but we reckon other layered materials could be used as well. The latter serves as a representative TMDC and it is chosen for the relatively good uniformity of ALD grown layers on top of it due to its higher concentration of vacancies[46,47] compared to other TMDCs. An aluminum oxide layer is subsequently grown on the layered material using ALD with ozone as a precursor (Fig. 1b) and pretreated with 10 cycles of ozone for 5s. The growth was performed at a temperature of 150 °C.

After the ALD growth, a secondary PDMS is used to exfoliate the as-grown alumina layer from the top while keeping the layered material on the primary PDMS (Fig. 1d). Using the deterministic transfer method[12], the exfoliated ALD grown metal oxide layer is transferred onto a target substrate (Fig. 1e). To prevent cracking during the transfer, we move the contact front slowly as these layers are less ductile than classical vdW materials. The amorphous nature of the grown material makes it prone to cracking as shown in Fig. 1i and these cracks appear along boundaries of areas with different number of layers on the template material. Thus, it is favorable to use larger crystals as template. However, the facility of the method is comparable to that of standard all-dry transfer and the yield of the exfoliation from the template is significantly higher. In addition, these challenges can be addressed through the implementation of automated assembly processes[13] and the use of wafer-sized 2D materials as templates.

Figure 1g, h shows atomic force microscopy (AFM) maps of the backside of alumina layer with root mean square (RMS) = 0.26 nm and the atomically smooth graphite template (RMS = 0.25 nm), respectively. The comparable values of roughness, which are at the resolution limit of the instrument, point to the fact that the backsize of the alumina layer is perfectly flat and thus creates a high-quality van-der-Waals interface with the target substrate. A micrograph (Fig. 1i) of the 8.7 nm thick Al_2O_3 with a lateral size of 37,528 μm^2 transferred onto a Si/SiO_2 wafer shows the robustness of this method. The size of the transferred flakes easily reaches ~ 10^4 μm^2, which is a size convenient for an assembly of various devices. It is limited by the size of the first layered materials used for the ALD growth and could be scaled up with larger layered materials in the future. The AFM image displayed in Fig. 1j shows the flat nature of the transferred flake with the measured surface RMS = 0.43 nm, which is significantly less than the measured surface RMS = 0.91 nm of the underlying Si/SiO_2 substrate. Supplementary Figure 1 shows micrographs of transferred Al_2O_3 on various substrates and stresses out the applicability of the method also to uneven surfaces. To characterize the nature of the ALD grown Al_2O_3, we performed X-ray photoelectron spectroscopy (XPS) and analyzed the binding energies of Al 2p (Fig. 1k) and O 1s (Fig. 1l) spectra. The Al 2p spectrum clearly shows one peak with the binding energy of 74.4 eV suggesting that the grown layer only comprises Al in the alumina form and no metallic aluminum is present. The O 1s spectrum may be deconvoluted into two distinct component peaks with binding energies of 531.15 eV and 532.47 eV. The first one corresponds to the Al-O bond and the latter likely comes from the surface adsorbed hydrogen forming a hydroxyl group. The absence of Al-OH peak in the Al 2p spectra with an energy of 75.3 eV[48] suggests that the film does not contain unreacted precursor and the -OH groups are only present on the surface of the film[49].

Consistent with previous findings[31,32], using water and trimethylaluminum (TMA) as a precursor leads to non-uniform growth on graphite substrate as shown in Supplementary Fig. 2. After 45 cycles, the Al_2O_3 is grown non-conformally from the sites of structural defects and layer edges. A film grown on WSe_2 with water as a precursor does not have the island-like morphology but features a number of pinholes. On the other hand with ozone as a precursor, the film is uniform and smooth both on graphite and WSe_2 with RMS of 0.12 nm and 0.13 nm respectively. To decrease the growth rate and grow very thin layers (such as in Fig. 1) we have grown alumina with first few cycles using ozone as a precursor after the pretreatment with ozone and then continuing the growth with H_2O as a precursor at the same temperature. Besides Al_2O_3, the method shall be applicable to the growth of other oxides. As examples, we showed the growth of ultra-thin layers of TiO_2 and ZnO by using this method in Supplementary Fig. 3.

DFT and XPS characterization

To understand the nature of the interaction of atoms in ALD growth and the principle of the exfoliation of the alumina, we performed the density-function theory (DFT) simulation (Fig. 2). We calculate the configurations of Al-terminated and O-terminated Al_2O_3 to provide insight into the character of the interface between alumina and 2D materials. The simulation of the binding energy between bilayer graphene and O-terminated Al_2O_3 as a function of distance shows that the exfoliation energy 32.67 meV A^{-2} of O-terminated Al_2O_3 is much larger than that of 12.44 meV A^{-2} for Al-terminated Al_2O_3. It is noted that the surface stability of the Al_2O_3 surface is given by its Gibbs free surface energy in which the Al-terminated Al_2O_3 surface is more thermodynamically favored[50]. A comparison with the graphene's interlayer exfoliation energy of 22.5 meV A^{-2} [18] could explain how the Al_2O_3 can be exfoliated without exfoliating the template material. The weak interaction can also be seen from the weak binding energy (see Fig. 2c), charge density redistribution (Fig. 2d), and preserved Dirac cone of graphene layers (Fig. 2f). In contrast, stronger interaction between bilayer graphene and O-terminated alumina leads to more profound charge density redistribution

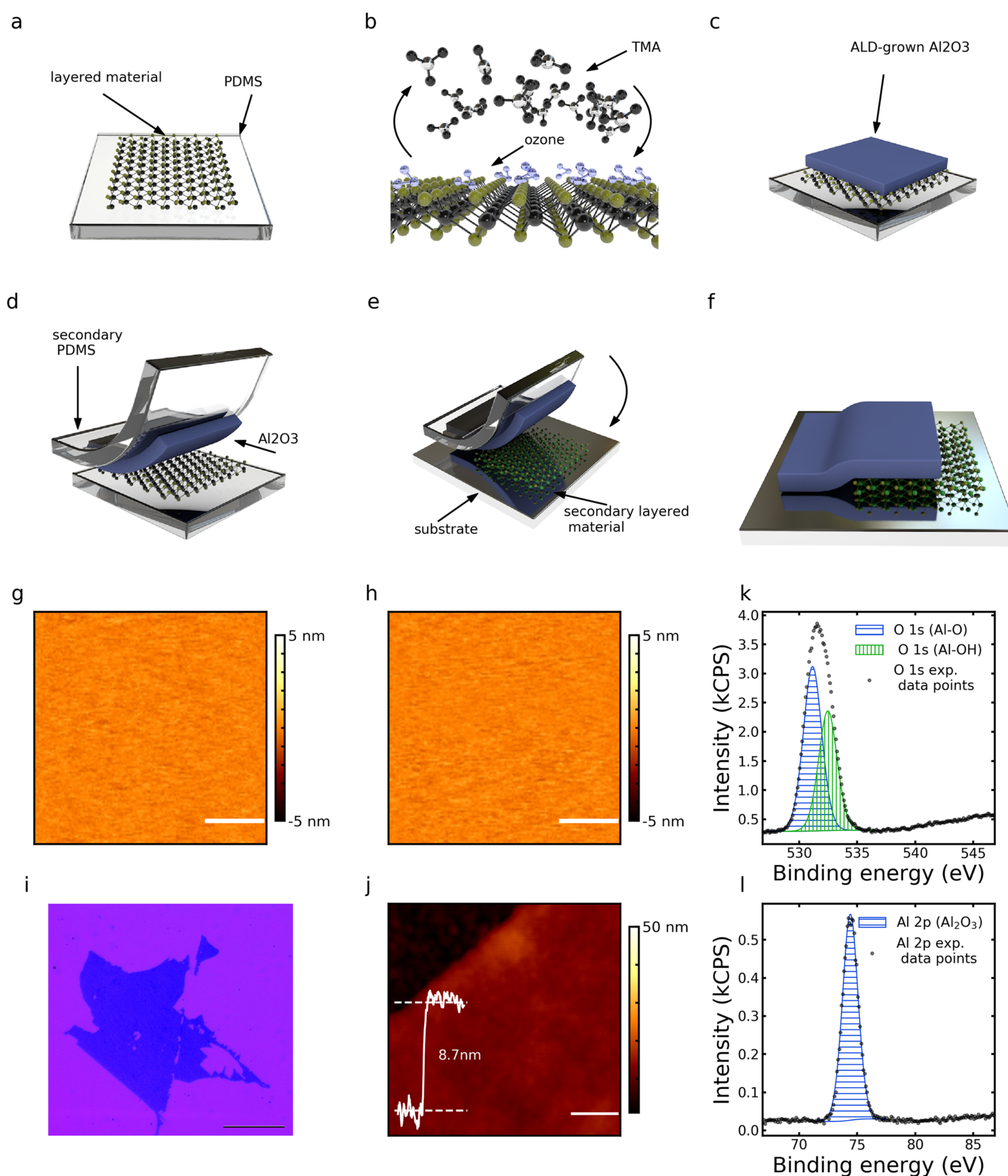

Fig. 1 Overview of the method. Firstly, a layered material is exfoliated onto PDMS (**a**), alumina is then ALD-grown onto it using O_3 as a precursor (**b**, **c**), a secondary piece of PDMS is used to exfoliate the as-grown alumina layer (**d**), and finally the alumina layer is placed onto a target substrate (**e**, **f**). AFM characterization of Al_2O_3 basal plane (RMS = 0.25 nm) (**g**) and graphite template (RMS = 0.24 nm) (**h**). Scalebars correspond to 50 nm. Characterization of the alumina layer by optical microscope (**i**) (scale bar corresponds to 50 µm), AFM (scale bar corresponds to 100 nm) (**j**) and and XPS analysis of O 1s (**k**) and Al 2p (**l**). The O 1s signal can be deconvoluted into two peaks corresponding to Al-O and Al-OH bonds.

(Fig. 2e) at the interface and band-gap opening in bilayer graphene. For WSe_2, the difference in the exfoliation energies with Al- and O-terminated Al_2O_3 is even more striking. The interlayer exfoliation energy of 25.6 meV A^{-2} [18] for WSe_2 is larger than that of 22.36 meV A^{-2} between WS_2 and Al terminated Al_2O_3, which is much smaller than that of 132.48 meV A^{-2} between WSe_2 and the O terminated Al_2O_3. Whereas the weak interaction between Al-terminated Al_2O_3 layer and bilayer WSe_2 preserves the electronic properties of WSe_2 as evidenced from the calculated local density of states (LDOS), stronger interaction with the O-terminated Al_2O_3 leads to the emergence of mid-gap states (Fig. 2g). Based on previous calculated Gibbs free energy of α-Al_2O_3 (0001)[50], it is found that Al-terminated Al_2O_3 (0001) surface is stable in a wide range of chemical potential. This suggests for the ALD deposited Al_2O_3 on the bilayer graphene and WSe_2, the Al-terminated Al_2O_3 will be more likely formed and its interaction with the 2D layers is relatively weak.

The DFT calculation and analysis of the nature of the interfacial interaction are supported by XPS shown in Fig. 3. Since the C1s in XPS spectra are often distorted by the presence of adventitious carbon and it becomes difficult to disentangle the signal coming from the graphite with that from the adventitious carbon[51], we focus our analysis on WSe_2. The Se 3d spectra are dominated by two peaks with binding energies of 54.69 eV and 55.57 eV

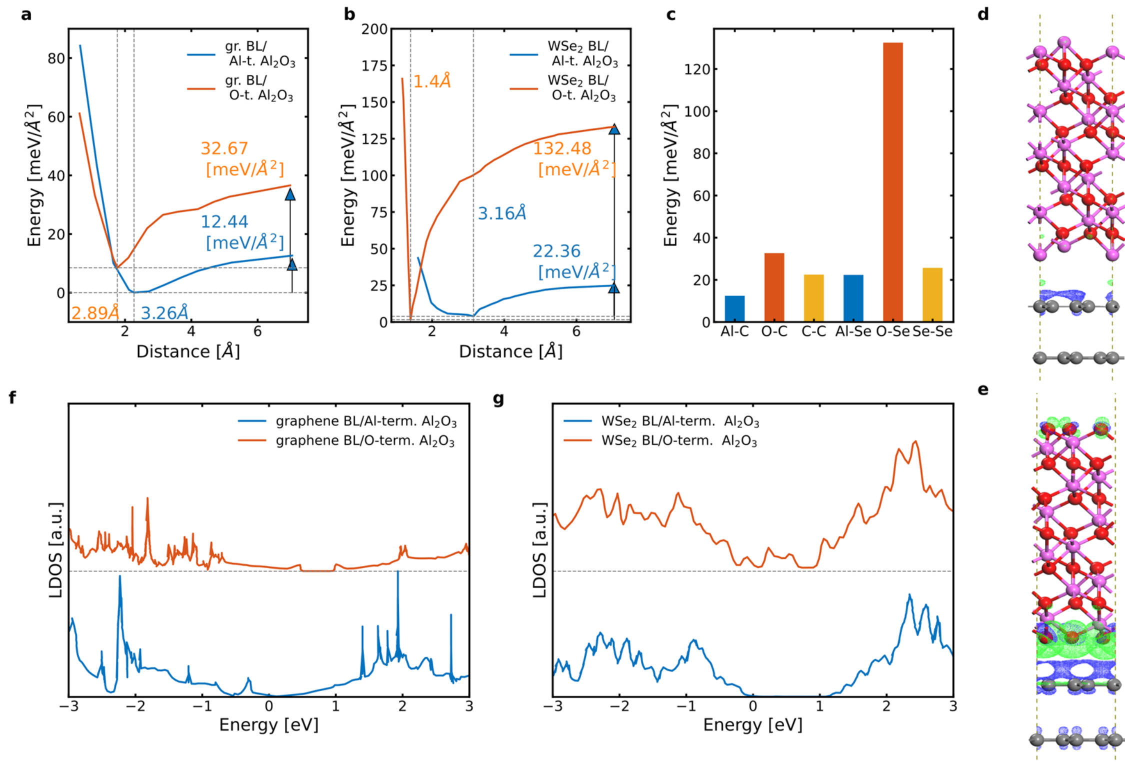

Fig. 2 The DFT simulation of the exfoliation energy of Al_2O_3 with bilayer graphene. (**a**) and bilayer WSe_2 (**b**). The calculated binding energy for O- and Al-terminated Al_2O_2 on bilayer graphene and WSe_2 (**c**). The charge density redistribution of bilayer graphene with Al-terminated (**d**) and O-terminated (**e**), shows the vdW nature of the interaction for Al-terminated and strong interaction for O-terminated Al_2O_3 on the template. Conversely, the local density of states graphs show preservation of the Dirac cone for bilayer graphene (**f**) and bandgap for bilayer WSe_2 (**g**) in the case of Al-terminated Al_2O_3 while interaction with O-terminated alumina leads to the introduction of a small bandgap opening and mid-gap states respectively. In these figures, green and blue dots denoted the charge depletion and accumulation, respectively, where the iso-surface value of 4.0×10^{-4} e Å^{-3} is used for the visualization.

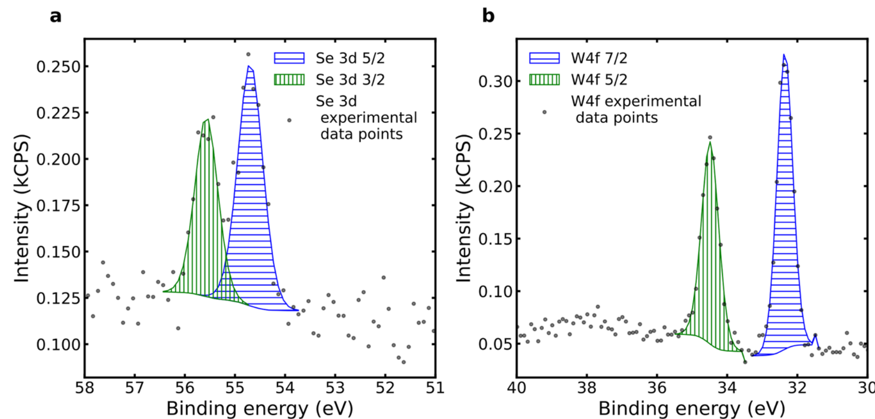

Fig. 3 XPS of WSe_2 below Al_2O_3 layer. Se 3d and W 4f XPS spectra obtained from WSe_2 with alumina grown on top shows absence of SeOx and WOx species. Se 3d spectrum (**a**) can be deconvoluted into two peaks corresponding to Se $3d_{5/2}$ and Se $3d_{3/2}$ respectively, while W 4f spestrum (**b**) corresponds to W $4f_{7/2}$ and W $4f_{5/2}$ lines.

corresponding to Se $3d_{5/2}$ and Se $3d_{3/2}$ respectively. The absence of peaks with the energy of 56.5 eV and 59-60 eV points to the absence of Se-O and SeOx species[52]. Similarly, the peaks with binding energies of 32.4 eV and 34.3 eV correspond to the W $4f_{7/2}$ and W $4f_{5/2}$ lines of WSe_2 and no WOx lines are observed[52–54]. As a control experiment, we pretreated the graphite and WSe_2 template with oxygen plasma and grew Al_2O_3. We then performed the exfoliation but the Al_2O_3 was exfoliated along with the underlying graphite and WSe_2 material (see Supplementary Fig. 4) instead of on its own as in the case of untreated template. It suggests that the underlying graphite and WSe_2 are oxidized and form a chemical bond with the grown alumina. The aforementioned analysis points to the existence of vdW interaction between Al-terminated Al_2O_3 and graphite or WSe_2 after the ALD growth.

2D materials encapsulation

We apply this method to encapsulate 2D materials in order to protect them from environmental degradation and to preserve

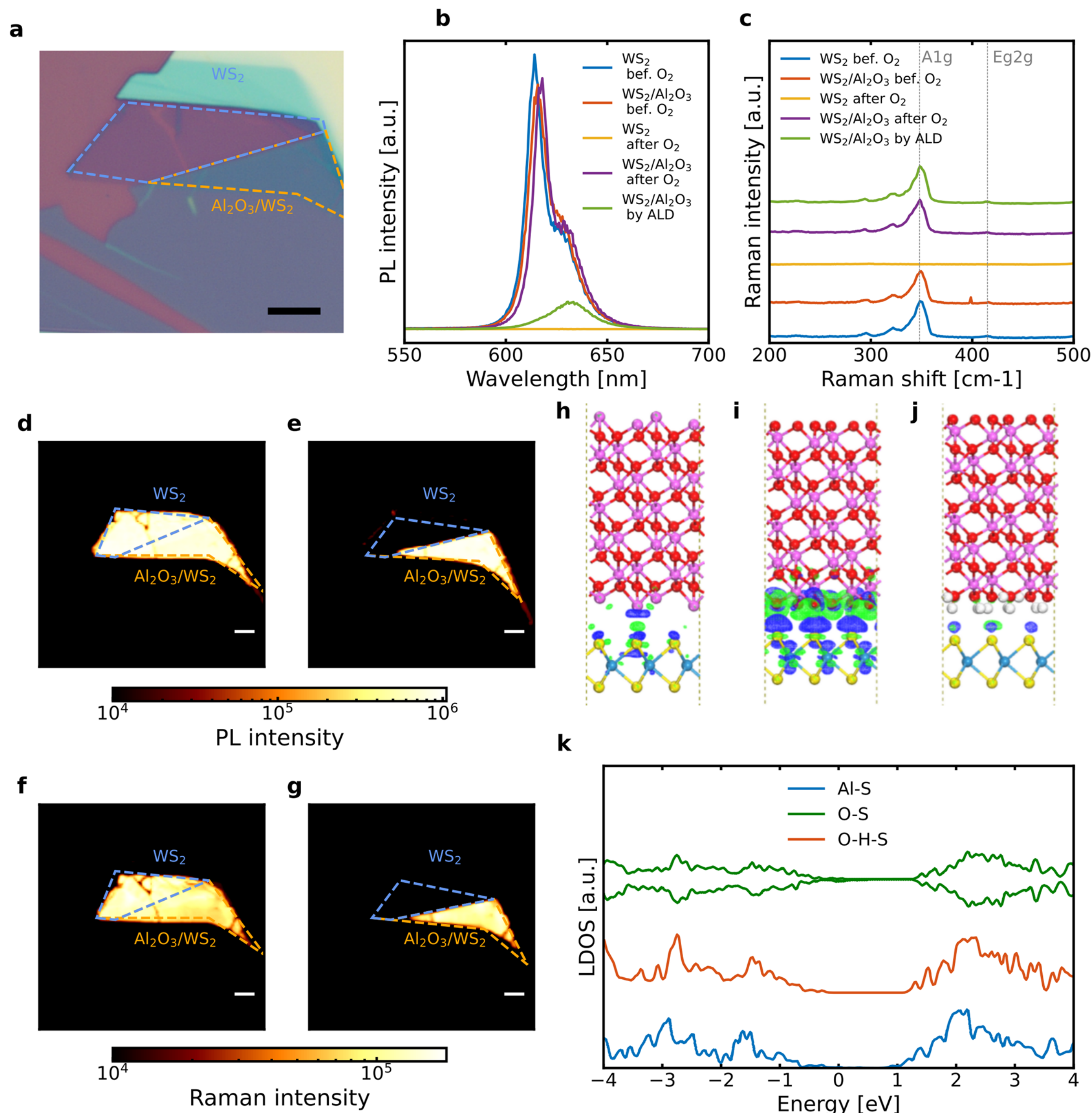

Fig. 4 Optical characterization of WS_2 with Al_2O_3 encapsulation. Micrograph (**a**) of a WS_2 monolayer encapsulated by a transferred 15 nm Al_2O_3 layer with PL (**b**) and Raman (**c**) spectra of encapsulated and non-encapsulated WS_2 monolayer before and after oxygen plasma treatment and that of WS_2 monolayer with ALD-grown alumina. Integrated PL (**d**, **e**) and Raman (**f**, **g**) maps are shown for the structure before and after plasma treatment respectively. (scale bars correspond to 10 μm) DFT simulation shows charge density redistribution (**h**–**j**) and LDOS (**k**) interface of WS_2 with Al-, O-terminated, and H-passivated O-terminated alumina.

solution-based processing. To demonstrate protection from oxidation and degradation even at extreme conditions we encapsulated part of the WS_2 monolayer flake by 15 nm Al_2O_3 layer grown on WSe_2 template (Fig. 4a) and treated it with 50 W oxygen plasma for 1 min at a pressure of 80 mTorr. We also compare it with WS_2 monolayer with alumina ALD grown directly on it by ALD. Figure 4b shows the PL spectra of WS_2 at different encapsulation conditions and different treatments, Fig. 4d, e shows the PL mapping of the sample encapsulated with Al_2O_3 before and after the plasma treatment respectively. While before the O_2 plasma treatment, the PL of the encapsulated WS_2 monolayer is slightly weaker than that of the non-encapsulated part, after the treatment the emission of the non-encapsulated part completely diminished while that of the encapsulated WS_2 monolayer did not change. We only observe a redshift of 1.6 nm and 3.8 nm for encapsulated WS_2 and encapsulated WS_2 after O_2 plasma respectively, which might be caused by charge screening by the Al_2O_3 layer. The fact that the PL intensity of the WS_2/Al_2O_3 heterostructure is not altered after the non-directional plasma treatment supports the assumption that the Al_2O_3 adheres well to the WS_2 monolayer via vdW interaction and creates a clean interface. On the other hand, direct ALD growth of alumina (with an equal thickness of 15 nm to the exfoliated alumina using O_3 as a precursor to achieve a conformal coverage) on a WS_2 monolayer leads to a significant quenching of PL. The fact that Raman peaks (Fig. 4c) of 348 cm^{-1} and 415 cm^{-1} corresponding to E_{2g} and A_{1g} modes of WS_2 are in the same positions and of similar intensity means that ozone treatment during ALD growth does not lead to a damage of the WS_2, but PL is 7x quenched due to doping of the material. This is consistent with the observed red-shift in the PL peak wavelength from 614.1 nm to 630.6 nm pointing to the transition from an exciton emission to a trion emission[55]. While the alumina on 2D materials mostly grows in the energetically favorable Al-terminated configuration as suggested above, the doping of WS_2 monolayer we observe indicates the existence of the stronger interfacial interaction as well.

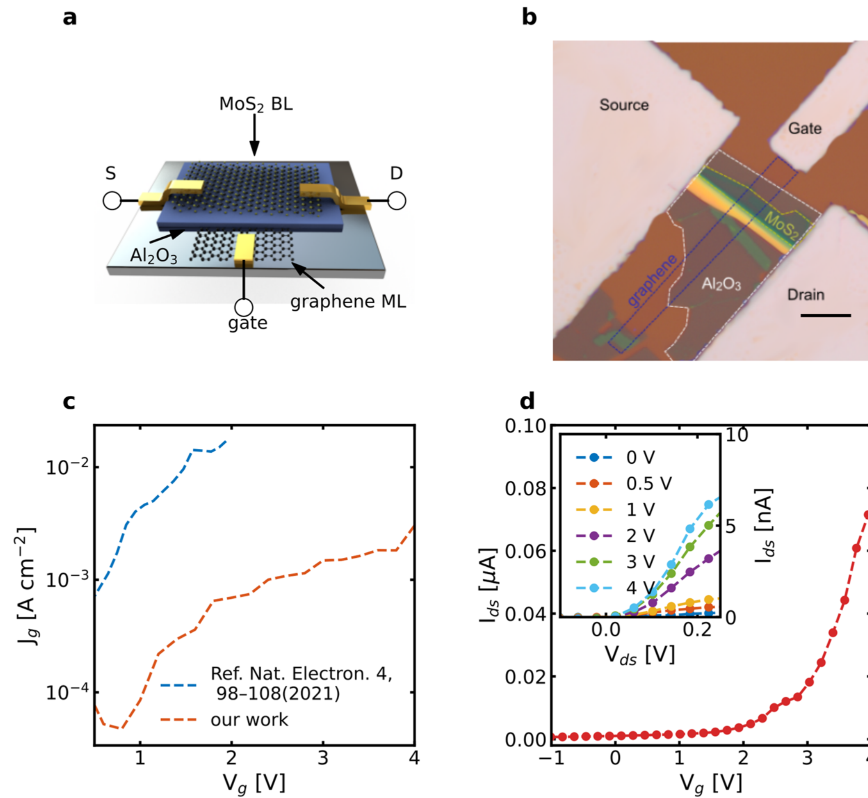

Fig. 5 MoS_2 based MOSFET with exfoliated alumina gate dielecric. The schematic drawing of the MOSFET (**a**) and micrograph (**b**) of a device comprised of a graphene gate, 15 nm thick transferred Al_2O_3 as a gate dielectric and a bilayer MoS_2 as the channel. The scalebar corresponds to 10 µm. Characteristic I_{ds}-V_g (**c**) and I_{ds}-V_g (inset of **c**) curves and gate leakage current compared to that of a device with 15 nm hBN[29] (**d**).

Using DFT, we analyzed the interface between O-terminated Al_2O_3 and WS_2, the same configuration with a sulfur vacancy, and an interface between O-terminated Al_2O_3 and WS_2 with hydrogen passivation in between. While the configurations of WS_2 with O-terminated Al_2O_3 and that with the S vacancy introduce mid-gap states, the configuration with hydroxyl-passivated Al_2O_3 leads to a weak interaction with WS_2 similar to that of the Al-terminated Al_2O_3. The hydrogen passivation, which we've revealed in Fig. 1i, then explains the absence of doping in the case of alumina transferred onto WS_2 and suggests the existence of an unperturbed Van der Waals interaction. Supplementary Fig. 5 shows the simulation of corresponding binding energies.

The disappearance of the Raman signal in non-encapsulated WS_2 after plasma treatment tells that the structural integrity of the monolayer is completely broken. Both E_{2g} and A_{1g} modes located at 348 cm^{-1} and 415 cm^{-1} respectively are clearly observable in the encapsulated WS_2 after the treatment as seen in Fig. 4f. No significant frequency shifts are observed suggesting that the alumina layer does not strain the WS_2 monolayer. We only observe a down-shift of $\delta\omega = 2\,cm^{-1}$ for the A_{1g} mode of WS_2 with a directly grown Al_2O_3 layer, while the position of E_{2g} mode remains unchanged. That is consistent with previous findings of A_{1g} down-shift in case of electrostatically doped MoS_2 bilayer[56]. To further analyze the straining of the encapsulated 2D material, we compared Raman spectra of MoS_2 encapsulated from both sides by exfoliated alumina and by hBN. We chose MoS_2 because of its sharp and easily distinguishable A_{1g} and E_{2g} modes. We observe a shift of 4.6 cm^{-1} in the case of a fully encapsulated MoS_2 monolayer in hBN and a shift of 2.2 cm^{-1} when placing MoS_2 monolayer onto exfoliated hBN. We observe only small shifts of 0.4 cm^{-1} and 1 cm^{-1} in case of encapsulation with alumina from one and both sides as shown in Supplementary Fig. 6. The encapsulation with the thin dielectric layer can be used to preserve the chemical treatment of the 2D materials as well (see Supplementary Fig. 7).

Fabrication of MOSFET device

In order to illustrate how the method could be utilized to fabricate devices, we have demonstrated a facile assembly of a metal-oxide-semiconductor field-effect transistor (MOSFET) device made of exfoliated alumina grown on WSe_2 template without the use of hBN. In the device (Fig. 5a, b), we used a 15 nm thick exfoliated alumina as the gate dielectric exploiting the high-κ nature of Al_2O_3, a graphene monolayer as the back gate, and a MoS_2 bilayer as the channel. Comparison to a similar MOSFET device with a 15 nm thick exfoliated hBN gate dielectric[29], our device shows approximately one order lower leakage current across the range of gate voltage as shown in Fig. 5d. Figure 5c shows I_{ds}-V_g at V_{ds} = 0.5 and I_{ds}-V_{ds} while the channel length L and width W are 24 µm and 2.1 µm respectively. The MoS_2 transistor has a clear n-type behavior with on/off ratio of ~ 10^3 and the I_{ds}-V_{ds} shows Schottky junction at the semiconductor/metal interface. While the calculated mobility (1.7 $cm^2V^{-1}s^{-1}$) does not reach the values reported for the best 2D materials-based devices[57–59], it is more than two orders of magnitude higher than an analogous device based on uncovered MoS_2 bilayer with Ti/Au Schottky contacts and SiO_2 as a gate dielectric[60]. We believe that the mobility could be further improved by careful optimization of the architecture, encapsulation of the device by a secondary layer of high-κ dielectric[57,58] or by fabrication of high-quality ohmic contacts such as those made of scandium[61], since Schottky barrier is a common problem for contacts to two-dimensional semiconductors[62,63].

Discussion

We have demonstrated a method for clean and facile integration of a thin dielectric layer into a vdW device. The dielectric layer is deposited by ALD on a layered template and subsequently transferred using a viscoelastic stamp. The high-quality transfer of the ALD Al_2O_3 thin layer is achievable due to the weak interaction between the deposited Al-terminated Al_2O_3 and the 2D materials as confirmed by a combination of DFT calculation and XPS measurement. Unlike previous methods, the presented technique using an atomically smooth template creates clean interface, which is essential for fabrication of vdW heterostructures. We have shown that this method preserves the optical properties of the WS_2 monolayer even after an aggressive plasma treatment without unintentional doping. A Van der Waals based MOSFET device with bilayer MoS_2 as the channel and transferred 15 nm thick alumina as the gate dielectric has a leakage current at least one magnitude lower than a similar MOSFET device using 15 nm hBN as a gate dielectric.

We believe that our method has a potential to be scaled up and utilized in a variety of ways in the future fabrication of large-scale 2D materials-based devices. Firstly, a combination with automatic self-assembly[13] and image recognition algorithms[64,65] could facilitate an easy integration into real-world devices. Secondly, instead of using exfoliated materials as templates and target substrate, chemical vapor deposition (CVD)-grown materials could be used perhaps in combination with one of the wafer-scale transfer methods[14,66,67]. Finally, the method would be suitable for devices with architectures different than the one we've showcased such as top-gated FET[58] or memristors[68].

METHODS

Materials and sample preparation

Crystals of MoS_2, WS_2, and hBN were purchased from 2Dsemiconductors and PDMS was purchased from gelpak. Samples of TMDs used in the work were mechanically exfoliated on PDMS and transferred using viscoelastic stamping. Contacts were fabricated with a standard photolithography followed by the deposition of 5 nm Ti/100 nm Au.

Atomic layer deposition

The atomic layer deposition was performed in Beneq TFS200. TMA and O_3 were used as precursors for the Al_2O_3 growth, tetrakis(dimethylamido)titanium and O_3 were used for the TiO_2 deposition, and diethylzinc and O_3 were used for the ZnO deposition. The growth of Al_2O_3 was performed at 150 °C or at 80 °C. Growth with the first five cycles using O_3 and then switching to H_2O was also tried. Purge times were 15 s for all precursors and all growths and pulse times were 200 ms.

Optical and electrical characterization

PL and Raman spectra were measured using Witec Alpha 300R confocal microscope. A 532 nm CW pump laser focused by a $\times 100$ microscope objective lens (NA $= 0.9$) was used for excitation and the emission was collected with the same objective. A diffraction grating with 150 lines/mm was used for photoluminescence spectroscopy and a diffraction grating with 1800 lines/mm was used for Raman spectroscopy. Liquid nitrogen cooled coupled charged device was used for the detection.

The electrical characterization was performed using Keithley 2410 and Keithley 2450 and controlled with the PyMeasure library.

Atomic force microscopy

Atomic Force Microscopy was performed on a Digital Instruments, Veeco Dimension 3100, under ambient conditions using Bruker probes TESP-V2 with a typical spring constant of 42 N m^{-1}. Operated in semi-contact mode with a pixel resolution 512x512 and a scan rate of ~ 1 Hz. Gwyddion 2.50 Revision 2018-02-02 and Python were used for scan analysis.

X-ray photoelectron spectroscopy

X-ray photoelectron spectroscopy was performed on a Thermo Scientific Theta Probe. X-ray Source: Monochromatic Al Kα X-ray ($\hbar\nu = 1486.7$ eV) X-ray spot: 400 µm in diameter. X-ray incident angle: 30° with respect to the surface normal. Photoelectrons take-off angle: 50° with respect to the surface normal. Charge compensation was achieved using low-energy electron flooding. Survey scans were used to confirm a lack of contaminate elements. Survey scan: step = 1 eV, Pass Energy = 200 eV, 1–5 scans. Narrow scan: Energy step = 0.1 eV, Pass Energy = 40 eV, 10^{-25} scans.

Density function theory calculation

The first-principles calculations were carried out by using density-functional theory based Vienna Ab initio Simulation Package (VASP.5.4.4.18)[69], in which the Perdew-Burke-Ernzerhof (PBE)[70] functional and the projector-augmented wave (PAW)[71] potentials were used for the exchange-correlation functionals and the interaction between electrons and core ions, respectively. In all the calculations, the cutoff energy for the plane wave expansion was set to 450 eV. Γ-centered $6 \times 6 \times 2$, $15 \times 15 \times 1$, and $12 \times 12 \times 1$ κ-point meshes were used to sample the first Brillouin zone of bulk Al_2O_3, bilayer graphene, and bilayer WSe_2 (WS_2), respectively. The interface structure of α-Al_2O_3 (0001) on bilayer graphene was modeled by placing slightly stretched Al_2O_3 (0001) on $(2 \times 2 \times 1)$ bilayer graphene, in which the first Brillouin zone was sampled by Γ-centered $6 \times 6 \times 1$ κ-point meshes. The interface structures of α-Al_2O_3 (0001) on bilayer WSe_2 (WS_2) were modeled by placing stretched (~2.2%) or compressed (~1.6%) $(2 \times 2 \times 1)$ α-Al_2O_3 (0001) on $(3 \times 3 \times 1)$ bilayer WSe_2 and bilayer WS_2, respectively, in which the first Brillouin zones were sampled by Γ-centered $3 \times 3 \times 1$ κ-point meshes. For all interface structures, we consider both Al- and O-terminated Al_2O_3 (0001) with symmetric surface terminations and thickness larger than 12 Å. A vacuum layer with a thickness of 15 Å was used for all interface structures to minimize the artificial Coulomb interaction between two adjacent surfaces. For the interface structures, the vdW correction was included by Grimme's DFT-D3 method[72], the spin-polarization effect was considered, and dipole correction was applied. For all calculations, the electronic and ionic convergence criteria were set to 10^{-5} eV and 0.01 eV Å^{-1}, respectively. The calculated lattice constants of α-Al_2O_3 and bilayer graphene, WSe_2 and WS_2 monolayer are $a = b = 4.814$ Å and $c = 12.991$ Å, and 2.465 Å, 3.276 Å, and 3.157 Å, respectively. The exfoliation energy is estimated by the energy difference between the interface structure in its equilibrium position and the interface structure with an interface spacing of 7 Å between Al_2O_3 and bilayer 2D materials. The interfacial interaction strength between Al_2O_3 and the bilayer 2D materials (graphene, WSe_2, and WS_2) can be estimated from the adsorption energy (E_{ad}) as defined below:

$$E_{ad} = E_{Al_2O_3+2D} - E_{Al_2O_3} - E_{2D} \quad (1)$$

where ($E_{Al_2O_3+2D}$) is the total energy of the interface structure for Al_2O_3 on the bilayer 2D materials, and $E_{Al_2O_3}$ and E_{2D} are the total energy of the isolated Al_2O_3 and bilayer 2D materials, respectively.

DATA AVAILABILITY

The data that support the findings of this study are available on request from the corresponding author.

Received: 10 August 2023; Accepted: 12 January 2024;
Published online: 08 February 2024

REFERENCES

1. Novoselov, K. S. et al. Electric field effect in atomically thin carbon films. *Science* **306**, 666–669 (2004).
2. Liu, Y. et al. Van der waals heterostructures and devices. *Nat. Rev. Mater.* **1**, 1–17 (2016).
3. Akinwande, D. et al. Graphene and two-dimensional materials for silicon technology. *Nature* **573**, 507–518 (2019).
4. Liu, Y. et al. Promises and prospects of two-dimensional transistors. *Nature* **591**, 43–53 (2021).
5. Schaibley, J. R. et al. Valleytronics in 2d materials. *Nat. Rev. Mater.* **1**, 1–15 (2016).
6. Wang, Z. et al. Greatly enhanced resonant exciton-trion conversion in electrically modulated atomically thin ws2 at room temperature. *Adv. Mater.* 2302248 (2023).
7. Wang, Z. et al. Exciton-enabled meta-optics in two-dimensional transition metal dichalcogenides. *Nano Lett.* **20**, 7964–7972 (2020).
8. Lau, C. S. et al. Dielectrics for two-dimensional transition-metal dichalcogenide applications. *ACS Nano* **17**, 9870–9905 (2023).
9. Schneider, G. F., Calado, V. E., Zandbergen, H., Vandersypen, L. M. & Dekker, C. Wedging transfer of nanostructures. *Nano Lett.* **10**, 1912–1916 (2010).
10. Pizzocchero, F. et al. The hot pick-up technique for batch assembly of van der waals heterostructures. *Nat. Commun.* **7**, 1–10 (2016).
11. Dean, C. R. et al. Boron nitride substrates for high-quality graphene electronics. *Nat. Nanotechnol.* **5**, 722–726 (2010).
12. Castellanos-Gomez, A. et al. Deterministic transfer of two-dimensional materials by all-dry viscoelastic stamping. *2D Mater.* **1**, 011002 (2014).
13. Masubuchi, S. et al. Autonomous robotic searching and assembly of two-dimensional crystals to build van der waals superlattices. *Nat. Commun.* **9**, 1–12 (2018).
14. Yu, H. et al. Wafer-scale growth and transfer of highly-oriented monolayer mos2 continuous films. *ACS nano* **11**, 12001–12007 (2017).
15. Quellmalz, A. et al. Large-area integration of two-dimensional materials and their heterostructures by wafer bonding. *Nat. Commun.* **12**, 1–11 (2021).
16. Kang, K. et al. Layer-by-layer assembly of two-dimensional materials into wafer-scale heterostructures. *Nature* **550**, 229–233 (2017).
17. Velicky, M. et al. Mechanism of gold-assisted exfoliation of centimeter-sized transition-metal dichalcogenide monolayers. *ACS Nano* **12**, 10463–10472 (2018).
18. Huang, Y. et al. Universal mechanical exfoliation of large-area 2d crystals. *Nat. Commun.* **11**, 1–9 (2020).
19. Liu, F. et al. Disassembling 2d van der waals crystals into macroscopic monolayers and reassembling into artificial lattices. *Science* **367**, 903–906 (2020).
20. Gramling, H. M. et al. Spatially precise transfer of patterned monolayer ws2 and mos2 with features larger than 104 μm2 directly from multilayer sources. *ACS Appl. Electron. Mater.* **1**, 407–416 (2019).
21. Du, K., Wathuthanthri, I., Liu, Y., Xu, W. & Choi, C.-H. Wafer-scale pattern transfer of metal nanostructures on polydimethylsiloxane (pdms) substrates via holographic nanopatterns. *ACS Appl. Mater. Interfaces* **4**, 5505–5514 (2012).
22. Kong, L. et al. Doping-free complementary wse 2 circuit via van der waals metal integration. *Nat. Commun.* **11**, 1–7 (2020).
23. Jung, Y. et al. Transferred via contacts as a platform for ideal two-dimensional transistors. *Nat. Electron.* **2**, 187–194 (2019).
24. Zhang, B. Y. et al. Hexagonal metal oxide monolayers derived from the metal–gas interface. *Nat. Mater.* **20**, 1073–1078 (2021).
25. Wierzbowski, J. et al. Direct exciton emission from atomically thin transition metal dichalcogenide heterostructures near the lifetime limit. *Sci. Rep.* **7**, 1–6 (2017).
26. Cadiz, F. et al. Excitonic linewidth approaching the homogeneous limit in mos 2-based van der waals heterostructures. *Phys. Rev. X* **7**, 021026 (2017).
27. Gorbachev, R. V. et al. Hunting for monolayer boron nitride: optical and raman signatures. *Small* **7**, 465–468 (2011).
28. Caldwell, J. D. et al. Photonics with hexagonal boron nitride. *Nat. Rev. Mater.* **4**, 552–567 (2019).
29. Knobloch, T. et al. The performance limits of hexagonal boron nitride as an insulator for scaled cmos devices based on two-dimensional materials. *Nat. Electron.* **4**, 98–108 (2021).
30. Vervuurt, R. H., Kessels, W. M. & Bol, A. A. Atomic layer deposition for graphene device integration. *Adv. Mater. Interfaces* **4**, 1700232 (2017).
31. Lee, B. et al. Conformal al 2 o 3 dielectric layer deposited by atomic layer deposition for graphene-based nanoelectronics. *Appl. Phys. Lett.* **92**, 203102 (2008).
32. Cheng, L. et al. Atomic layer deposition of a high-k dielectric on mos2 using trimethylaluminum and ozone. *ACS applied materials & interfaces* **6**, 11834–11838 (2014).
33. Jandhyala, S. et al. Atomic layer deposition of dielectrics on graphene using reversibly physisorbed ozone. *ACS Nano* **6**, 2722–2730 (2012).
34. Vervuurt, R. H., Karasulu, B., Verheijen, M. A., Kessels, W. E. M. & Bol, A. A. Uniform atomic layer deposition of al2o3 on graphene by reversible hydrogen plasma functionalization. *Chem. Mater.* **29**, 2090–2100 (2017).
35. Lee, B. et al. Characteristics of high-k al2o3 dielectric using ozone-based atomic layer deposition for dual-gated graphene devices. *Appl. Phys. Lett.* **97**, 043107 (2010).
36. Yun, T. et al. Influence of direct deposition of dielectric materials on the optical response of monolayer ws2. *Appl. Phys. Lett.* **119**, 133106 (2021).
37. Leonhardt, A. et al. Material-selective doping of 2d tmdc through al x o y encapsulation. *ACS Appl. Mater. Interfaces* **11**, 42697–42707 (2019).
38. McClellan, C. J., Yalon, E., Smithe, K. K., Suryavanshi, S. V. & Pop, E. High current density in monolayer mos2 doped by alo x. *ACS Nano* **15**, 1587–1596 (2021).
39. Lau, C. S. et al. Carrier control in 2d transition metal dichalcogenides with al 2 o 3 dielectric. *Sci. Rep.* **9**, 1–6 (2019).
40. Kim, S. et al. Realization of a high mobility dual-gated graphene field-effect transistor with al 2 o 3 dielectric. *Appl. Phys. Lett.* **94**, 062107 (2009).
41. Fallahazad, B., Kim, S., Colombo, L. & Tutuc, E. Dielectric thickness dependence of carrier mobility in graphene with hfo 2 top dielectric. *Appl. Phys. Lett.* **97**, 123105 (2010).
42. Mackus, A., Bol, A. & Kessels, W. The use of atomic layer deposition in advanced nanopatterning. *Nanoscale* **6**, 10941–10960 (2014).
43. Huang, J.-K. et al. High-κ perovskite membranes as insulators for two-dimensional transistors. *Nature* **605**, 262–267 (2022).
44. Yang, A. J. et al. Van der waals integration of high-κ perovskite oxides and two-dimensional semiconductors. *Nat. Electron.* **5**, 233–240 (2022).
45. Illarionov, Y. Y. et al. Insulators for 2d nanoelectronics: the gap to bridge. *Nat. Commun.* **11**, 1–15 (2020).
46. Amani, M. et al. Recombination kinetics and effects of superacid treatment in sulfur-and selenium-based transition metal dichalcogenides. *Nano Lett.* **16**, 2786–2791 (2016).
47. Park, T. et al. Atomic layer deposition of al 2 o 3 on mos 2, ws 2, wse 2, and h-bn: surface coverage and adsorption energy. *RSC Adv.* **7**, 884–889 (2017).
48. Yoon, K. H., Kim, H., Lee, Y.-E. K., Shrestha, N. K. & Sung, M. M. Uv-enhanced atomic layer deposition of al 2 o 3 thin films at low temperature for gas-diffusion barriers. *RSC Adv.* **7**, 5601–5609 (2017).
49. Fang, R.-C. et al. High-performance bilayer flexible resistive random access memory based on low-temperature thermal atomic layer deposition. *Nanoscale Res. Lett.* **8**, 1–7 (2013).
50. Kresse, G. et al. Structure of the ultrathin aluminum oxide film on nial (110). *Science* **308**, 1440–1442 (2005).
51. Barr, T. L. & Seal, S. Nature of the use of adventitious carbon as a binding energy standard. *J. Vac. Sci. Technol. A* **13**, 1239–1246 (1995).
52. Azcatl, A. et al. Hfo2 on uv–o3 exposed transition metal dichalcogenides: interfacial reactions study. *2D Mater.* **2**, 014004 (2015).
53. Kang, W.-M. et al. Multi-layer wse2 field effect transistor with improved carrier-injection contact by using oxygen plasma treatment. *Solid State Electron.* **140**, 2–7 (2018).
54. Azcatl, A., Wang, Q., Kim, M. J. & Wallace, R. M. Al2o3 on wse2 by ozone based atomic layer deposition: Nucleation and interface study. *APL Mater.* **5**, 086108 (2017).
55. Plechinger, G. et al. Identification of excitons, trions and biexcitons in single-layer ws2. *Phys. Status Solidi - Rapid Res. Lett.* **9**, 457–461 (2015).
56. Lu, X. et al. Gate-tunable resonant raman spectroscopy of bilayer mos2. *Small* **13**, 1701039 (2017).
57. Wang, H. et al. Integrated circuits based on bilayer mos2 transistors. *Nano Lett.* **12**, 4674–4680 (2012).
58. Radisavljevic, B., Radenovic, A., Brivio, J., Giacometti, V. & Kis, A. Single-layer mos 2 transistors. *Nat. Nanotechnol.* **6**, 147–150 (2011).
59. Chow, W. L. et al. High mobility 2d palladium diselenide field-effect transistors with tunable ambipolar characteristics. *Adv. Mater.* **29**, 1602969 (2017).
60. Di Bartolomeo, A. et al. Asymmetric schottky contacts in bilayer mos2 field effect transistors. *Adv. Func. Mater.* **28**, 1800657 (2018).
61. Das, S., Chen, H.-Y., Penumatcha, A. V. & Appenzeller, J. High performance multilayer mos2 transistors with scandium contacts. *Nano Lett.* **13**, 100–105 (2013).
62. Allain, A., Kang, J., Banerjee, K. & Kis, A. Electrical contacts to two-dimensional semiconductors. *Nat. Mater.* **14**, 1195–1205 (2015).
63. Kim, C. et al. Fermi level pinning at electrical metal contacts of monolayer molybdenum dichalcogenides. *ACS Nano* **11**, 1588–1596 (2017).
64. Masubuchi, S. & Machida, T. Classifying optical microscope images of exfoliated graphene flakes by data-driven machine learning. *Npj 2D Mater. Appl.* **3**, 4 (2019).
65. Masubuchi, S. et al. Deep-learning-based image segmentation integrated with optical microscopy for automatically searching for two-dimensional materials. *Npj 2D Mater. Appl.* **4**, 3 (2020).
66. Kim, Y. et al. Tailored graphene micropatterns by wafer-scale direct transfer for flexible chemical sensor platform. *Adv. Mater.* **33**, 2004827 (2021).

67. Shivayogimath, A. et al. Do-it-yourself transfer of large-area graphene using an office laminator and water. *Chem. Mater.* **31**, 2328–2336 (2019).
68. Huh, W., Lee, D. & Lee, C.-H. Memristors based on 2d materials as an artificial synapse for neuromorphic electronics. *Adv. Mater.* **32**, 2002092 (2020).
69. Kresse, G. & Hafner, J. Ab initio molecular dynamics for liquid metals. *Phys. Rev. B* **47**, 558 (1993).
70. Perdew, J. P., Burke, K. & Ernzerhof, M. Generalized gradient approximation made simple. *Phys. Rev. Lett.* **77**, 3865 (1996).
71. Blöchl, P. E. Projector augmented-wave method. *Phys. Rev. B* **50**, 17953 (1994).
72. Wu, X., Vargas, M., Nayak, S., Lotrich, V. & Scoles, G. Towards extending the applicability of density functional theory to weakly bound systems. *J. Chem. Phys.* **115**, 8748–8757 (2001).

ACKNOWLEDGEMENTS

MS thanks UCL and the ARAP program of A*STAR for the scholarship and facilities. The work is supported by the Agency for Science, Technology and Research (A*STAR) under IRG Program (Grant Nos. A2083c0058, A20E5c0084), IAF-PP Program, (Grant no. H19H6a0025), the National Research Foundation, Singapore under NRF-CRP (NRF-CRP26-2021-0004). M.Y would like to thank the funding support (project numbers: 1-BE47 and ZE2F) from The Hong Kong Polytechnic University and Center for Advanced 2D Materials and Graphene Research at National University of Singapore for providing computing resources. We acknowledge Meltem Yilmaz for fruitful discussions on atomic layer deposition.

AUTHOR CONTRIBUTIONS

M.S and Z.W. contributed equally to this work. M.S., Z.W. and J.T. conceived the project. M.S. fabricated the samples. Z.W. and M.S. characterized the MOSFET device and performed the PL and Raman mapping. N.G.W. performed the AFM mapping and XPS analysis. M.Y. performed the DFT simulations. D.C.J.N. helped with the ALD deposition. S.W., J.P., N.T.K.T. and J.T. supervised the project. M.S. and Z.W. wrote the manuscript; all the authors revised and commented on the manuscript. All authors contributed to the writing of manuscript and interpretation of the data.

COMPETING INTERESTS

The authors declare no competing interests.

ADDITIONAL INFORMATION

Supplementary information The online version contains supplementary material available at https://doi.org/10.1038/s41699-024-00443-2.

Correspondence and requests for materials should be addressed to Matej Sebek, Ming Yang, Nguyen Thi Kim Thanh or Jinghua Teng.

Reprints and permission information is available at http://www.nature.com/reprints

Publisher's note Springer Nature remains neutral with regard to jurisdictional claims in published maps and institutional affiliations.

Open Access This article is licensed under a Creative Commons Attribution 4.0 International License, which permits use, sharing, adaptation, distribution and reproduction in any medium or format, as long as you give appropriate credit to the original author(s) and the source, provide a link to the Creative Commons license, and indicate if changes were made. The images or other third party material in this article are included in the article's Creative Commons license, unless indicated otherwise in a credit line to the material. If material is not included in the article's Creative Commons license and your intended use is not permitted by statutory regulation or exceeds the permitted use, you will need to obtain permission directly from the copyright holder. To view a copy of this license, visit http://creativecommons.org/licenses/by/4.0/.

© The Author(s) 2024